



**Low-Reflection, (110)-Orientation-Preferred CsPbBr<sub>3</sub>  
Nanonet Films for Application in High-Performance  
Perovskite Photodetectors**

Journal:	<i>Nanoscale</i>
Manuscript ID	NR-COM-04-2019-003213
Article Type:	Communication
Date Submitted by the Author:	15-Apr-2019
Complete List of Authors:	Liu, Ronghuan ; Hubei University Zhou, Hai; Hubei University, Faculty of Physics and Electronic Technology Wuhan Song, Zhaoning; University of Toledo, Physics and Astronomy Yang, Xiaohan; Hubei University Wu, Dingjun; Hubei University Song, Zehao; Faculty of Physics and Electronic Science, Hubei University, Wang, Hao; Hubei University, Faculty of Physics and Electronic Technology Yan, Yanfa; University of Toledo, Department of Physics and Astronomy

# Low-Reflection, (110)-Orientation-Preferred CsPbBr<sub>3</sub> Nanonet Films for Application in High-Performance Perovskite Photodetectors

Ronghuan Liu,<sup>†</sup> Hai Zhou,<sup>†,\*</sup> Zhaoning Song,<sup>‡</sup> Xiaohan Yang,<sup>†</sup> Dingjun Wu,<sup>†</sup>  
Zehao Song,<sup>†</sup> Hao Wang,<sup>†,\*</sup> and Yanfa Yan<sup>‡,\*</sup>

<sup>†</sup>Hubei Key Laboratory of Ferro & Piezoelectric Materials and Devices, Faculty of Physics & Electronic Science, Hubei University, Wuhan, 430062, P.R. China.

<sup>‡</sup>Department of Physics and Astronomy and Wright Center for Photovoltaics Innovation and Commercialization, The University of Toledo, Toledo, Ohio, 43606, USA.

Corresponding Author

A/Prof. Hai Zhou: [hizhou34@126.com](mailto:hizhou34@126.com)

Prof. Hao Wang: [nanoguy@126.com](mailto:nanoguy@126.com)

Prof. Yanfa Yan: [Yanfa.Yan@utoledo.edu](mailto:Yanfa.Yan@utoledo.edu)

**ABSTRACT**

All-inorganic metal halide perovskites have caught great interest in recent years due to their good device performance with higher thermal stability than their organic-inorganic perovskite counterparts. However, the all-inorganic perovskite polycrystalline films prepared by the conventional spin-coating method possess many pinholes, nonuniform surface with many small crystals, and irregular agglomerates, limiting their device performance. Herein, we introduced a monolayer nano-polystyrene (PS) sphere confined growth method for obtaining CsPbBr<sub>3</sub> nanonet films (NFs) with ordered nanostructures grown in the preferred (110) orientation, which benefits for the charge carrier transport and the light-harvesting efficiency. The (110) peak intensity of CsPbBr<sub>3</sub> NFs increased with increasing the diameter of the monolayer sphere, while the (001) peak intensity was suppressed greatly, indicating the more preferred (110) orientated growth. The PDs based on (110)-orientation-preferred CsPbBr<sub>3</sub> NFs prepared by using 850 nm PS spheres showed the best performance. The best performing device displayed the biggest linear dynamic range of up to 120 dB. In addition, the responsivity of 2.84 A W<sup>-1</sup> and the detectivity of 5.47×10<sup>12</sup> Jones were also achieved.

**KEYWORDS:** CsPbBr<sub>3</sub>, perovskite, photodetector, nanonet, confined growth

Organic-inorganic metal halide perovskites are a class of compounds whose molecular formula can be expressed as  $ABX_3$  (A=methylammonium (MA), formamidinium (FA); B = Pb, Sn; X = Cl, Br, I). These materials have exhibited attractive applications in the fields of solar cells, photodetectors (PDs), and light-emitting diodes (LEDs) due to their tunable band gaps, high light absorption coefficients, and long carrier diffusion lengths [1-4]. Up to now, the certified efficiency of the solar cells based on organic-inorganic metal halide perovskites has exceeded 23.7% [1], and the external quantum efficiency of the LEDs with perovskites as an active material has achieved more than 20% [2, 3]. Besides, the detectivity of the PDs using the two-dimensional perovskite nanowire arrays has been as high as  $7 \times 10^{15}$  Jones [4]. However, such halide perovskite materials typically suffer from poor device stability due to the compositions containing poorly stable organic cations, limiting their wide applications in optoelectronic devices.

Compared to the organic-inorganic perovskites, their all-inorganic Cs-based counterparts, especially  $CsPbBr_3$ , have caught great interest due to their good device performance with higher thermal stability [5-12]. Yang and coauthors [11] reported a low temperature and substrate-independent growth method for growing millimeter-size inorganic perovskite monocrystalline thin films, which exhibited excellent long-term stability against humidity and thermal stress, and the as-grown  $CsPbBr_3$  monocrystalline film PDs with the metal-semiconductor-metal (MSM) structure displayed high photodetection performance with the responsivity of  $2.5 \text{ A W}^{-1}$ , on/off ratio of  $\approx 10^3$ , and the rise and decay time of 0.4 and 9 ms, respectively. Besides, Saidaminov and coauthors [12] reported the phase-selective low-temperature growth of inorganic lead halide perovskite single crystals, and their self-powered PDs showed a specific detectivity of  $1.7 \times 10^{11}$  Jones, an on/off ratio of  $10^5$ , and rise/decay times of 230/60 ms at zero bias. Despite the exciting progress in these  $CsPbBr_3$  PDs, it is still difficult to accurately control the thickness and size of single crystals [11, 13,14].

An alternative approach is to use polycrystalline films prepared by a simple solution process that possesses better controllability and adjustability and is possible to scale up production in industrial fabrication, endowing polycrystalline perovskites with great potential for optoelectronic applications [15,16]. Generally, the CsPbBr<sub>3</sub> polycrystalline films prepared by the conventional one-step spin-coating method contain many pinholes, nonuniform surface, small crystals, and irregular agglomerates due to the poor solubility of CsPbBr<sub>3</sub> in dimethylsulfoxide (DMSO) [17, 18]. Additionally, the spin-coated CsPbBr<sub>3</sub> films exhibit the perovskite phase with a preferred orientation in the (100) direction, and are typically accompanied with a strong peak of PbBr<sub>2</sub> [19, 20]. Too much of the PbBr<sub>2</sub> phase is believed to be undesirable for carrier transport and device performance [21]. Zuo et al. reported [22] that the MAPbBr<sub>3</sub> single crystal PDs based on the (110) plane-oriented perovskites showed a 153.33% enhancement of responsivity compared to that of the device based on perovskites with the (100) orientation. They attributed the enhanced performance to coincidence of the direction of electric field applied to the device, which is on the (110) surface, and the defects' favorite migration path, which benefits the carrier transport. Qi's group [23] reported on the MAPbI<sub>3</sub> perovskite nanonets fabricated by using monolayer colloidal crystal templates with a strong intensity of the (112) peak, which showed the highest photocurrent compared with other thin-film counterparts in different crystal orientations. These results indicate that depressing the (100) orientation of the perovskite film may provide an effective avenue to obtain better device performance.

In this paper, we use a monolayer nano-polystyrene (PS) sphere confined growth method for obtaining (110)-orientation-preferred CsPbBr<sub>3</sub> films with ordered nanostructures, which can efficiently reduce the optical reflection and enhance the light-harvesting efficiency, benefitting the device performance. Based on the monolayer nano-PS confined growth method with various size spheres, the degree of preferred orientation on the (110) plane of CsPbBr<sub>3</sub> nanonet films (NFs) increases with increasing the diameter of the monolayer sphere. The PDs based on

(110)-orientation-preferred CsPbBr<sub>3</sub> NFs prepared by using 850 nm PS spheres show the best performance. The best-performing PD displays a biggest linear dynamic range (LDR) of up to 120 dB. In addition, the responsivity and detectivity of 2.84 A W<sup>-1</sup> and 5.47×10<sup>12</sup> Jones are also achieved.

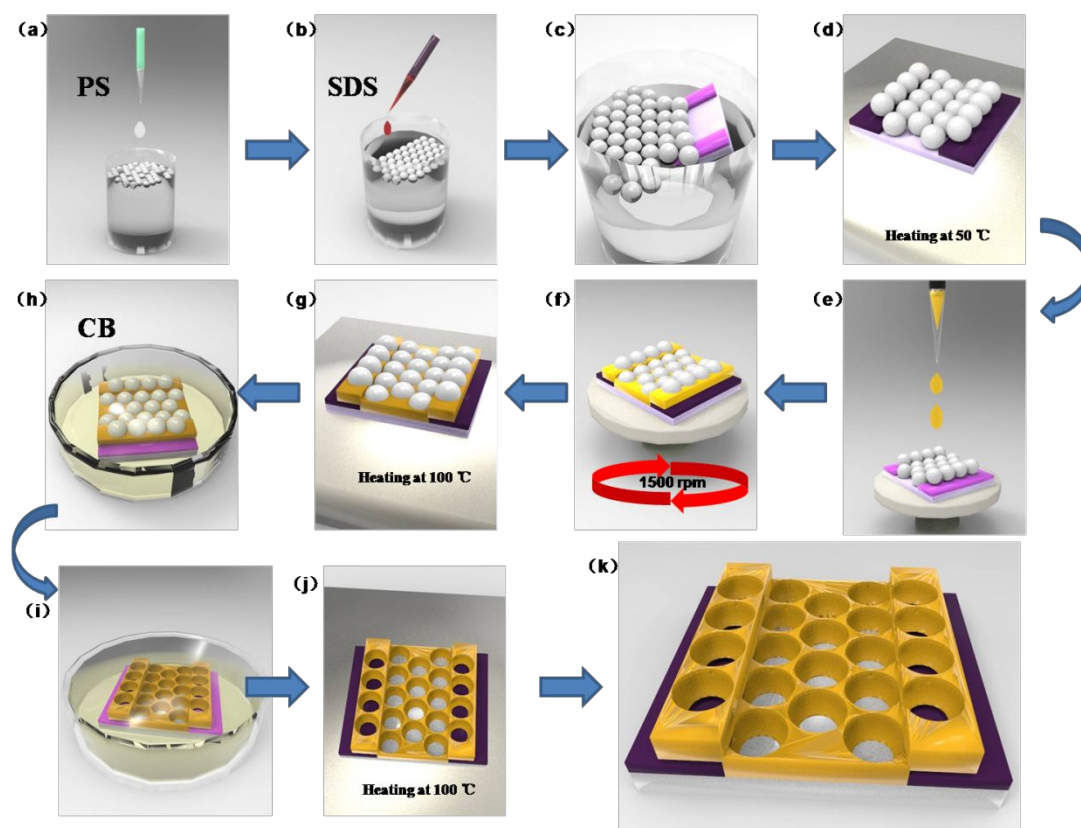


Figure 1 Schematic illustration of the synthesis process of the CsPbBr<sub>3</sub> NFs.

Figure 1 illustrates the synthesis process for the CsPbBr<sub>3</sub> NFs. First, the PS in ethanol solution was dropped to a beaker filled with water by using a plastic pipette and spread uniformly on the water surface (Figure 1a). Then, 1 mL sodium dodecyl sulfate (SDS) solution was dropped along the edge of the glass beaker (Figure 1b) to reduce the gaps among the PS spheres. White PS spheres aggregated quickly at the opposite side of the glass beaker, forming a suspension of a uniform PS layer in the water. After that, an ultraviolet-ozone treated glass substrate with patterned FTO electrodes was inserted into the water under the PS layer from the edge of the PS layer (Figure 1c), and slowly picked up vertically to transfer the PS layer to the substrate.

Then the substrate with a monolayer of PS was placed on a hot plate at 50 °C and kept for 1 h (Figure 1d). To deposit the perovskite film, a 70  $\mu\text{L}$  CsPbBr<sub>3</sub> DMSO solution (0.5 mol/L) was added drop by drop onto the PS coated FTO substrate (Figure 1e) and spin-coated at 1500 rpm for 40 s (Figure 1f). The substrate was then baked on a hot plate at 100 °C for 30 min (Figure 1g). After cooling down, the substrate was immersed in chlorobenzene for 1 min to remove the PS spheres (Figure 1h and 1i). The substrate was then taken out of the solution and baked at 100°C for 30 min to remove chlorobenzene (Figure 1j). Finally, the CsPbBr<sub>3</sub> nanonet films with an active area of  $3.5 \times 0.08 \text{ mm}^2$  were prepared (Figure 1k).

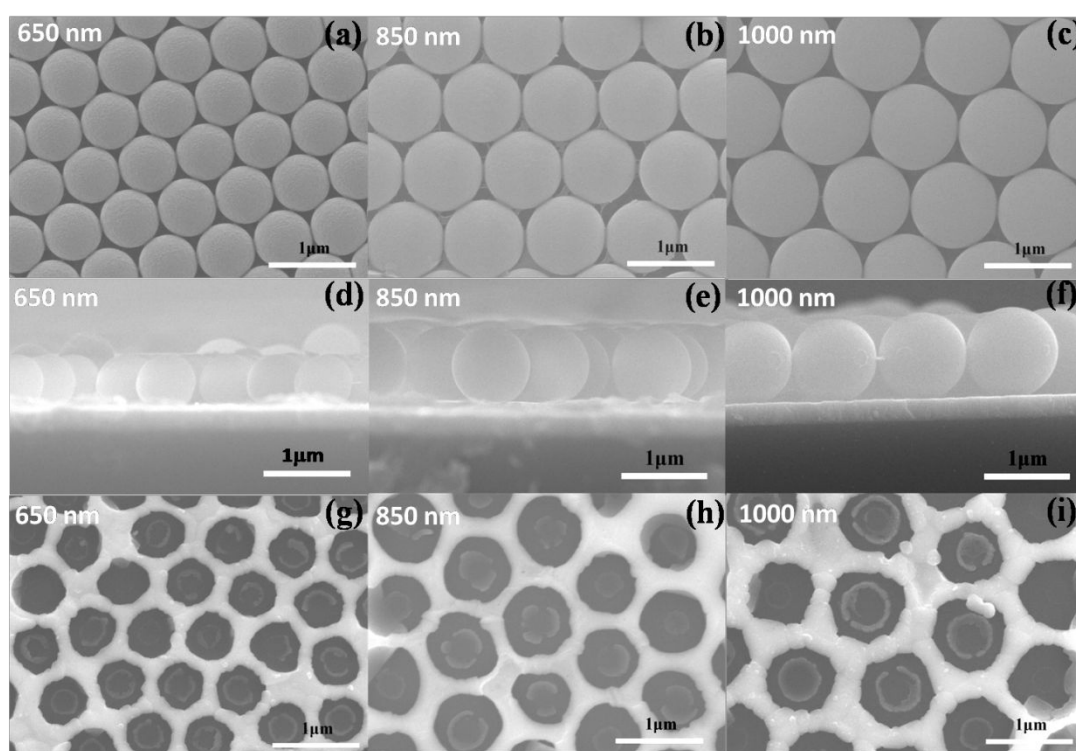


Figure 2 Top SEM images of the PS spheres with diameters of (a) 650 nm, (b) 850 nm and (c) 1000 nm. Cross sectional SEM images of the PS spheres with diameters of (d) 650 nm, (e) 850 nm and (f) 1000 nm. Top view of the SEM images of the CsPbBr<sub>3</sub> prepared with PS diameters of (g) 650 nm, (h) 850 nm and (i) 1000 nm. The scale bars are 1  $\mu\text{m}$ .

Figure 2 and Figure S1 show the scanning electron microscopy (SEM) images of the PS and CsPbBr<sub>3</sub> perovskite NFs. All PS spheres with various diameters can be grown uniformly on the FTO glass substrate (Figure 2 a-c). The monolayer PS spheres can be seen clearly from the cross-sectional SEM images, as shown in Figure 2d-2f. After spin-coating the CsPbBr<sub>3</sub> precursor solution and removing the PS spheres, the NFs can be formed with nanoholes of various sizes, shown in Figure 2g-2i. In our experiments, the PS templates with the diameter ranging from 250 to 1150 nm were used, and the NFs with various nanoholes were prepared with large grain sizes and smooth surfaces. As revealed by the SEM images, the diameters of the nanoholes are slightly shorter than that of the corresponding PS spheres. It is worth noting that the homogeneous and compact CsPbBr<sub>3</sub> NF is better than the traditionally spin-coated films, which show many pinholes, unordered surface with many small crystals and irregular agglomerates (Figure S2), limiting the device performance.

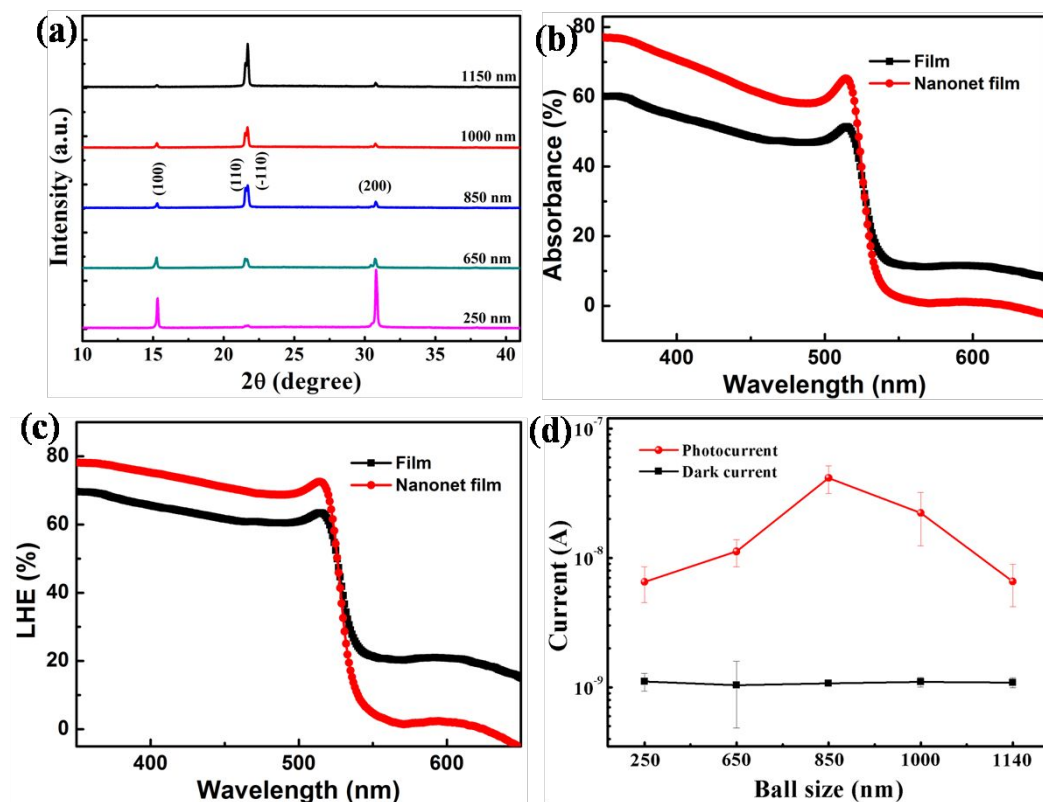


Figure 3 (a) XRD patterns of the CsPbBr<sub>3</sub> NFs. (b) Absorption characteristic and (c) light-harvesting efficiency (LHE) of traditionally spin-coated CsPbBr<sub>3</sub> film and CsPbBr<sub>3</sub> nanonet film. The LHE can be expressed as  $LHE(\lambda) = (1-R) \times (1-10^{-A(\lambda)})$ , R is the reflectance and  $A(\lambda)$  is the absorbance. (d) Dark- and photo-current of the CsPbBr<sub>3</sub> NF PDs prepared with various PS spheres. The DC bias is 2 V and the light intensity is about 1.45 mW cm<sup>-2</sup>.

More interestingly, we find that the monolayer nano-sphere confined growth of CsPbBr<sub>3</sub> NFs not only leads to less morphological defects but also favors the (110) orientation of crystals. From X-ray diffraction (XRD) patterns of the CsPbBr<sub>3</sub> NFs shown in Figure 3a, the peaks located at 15.3°, 21.5°, 21.7° and 30.8° can be assigned to the (100), (110), (-110), and (200) crystal planes, respectively, indicating a typical orthorhombic structure of CsPbBr<sub>3</sub> [19, 20]. It shows clearly that with increasing the PS sphere diameter, the intensity of the (100) orientation decreases and the (110) and (-110) intensities increase, indicating that the (100) orientation can be depressed by increasing the diameter of the PS templates and the preferred growth orientations are along the (110) and (-110) planes. To clearly see the changes of the (110) orientation, the partially amplified XRD patterns of the CsPbBr<sub>3</sub> NFs are shown in Figure S3. The increment of the (110) orientation reaches the maximum value with the PS sphere diameter of 850 nm. To accurately express the growth orientation, the relationship of the peak ratio of the intensity ( $I_{(110)}/I_{(100)}$ ) versus the diameter of the PS is shown in Figure S4. When the sphere size increases from 250 to 1150 nm, the ratio of  $I_{(110)}/I_{(100)}$  increases from 0.1 to 8.6, all of which are larger than that of the traditionally spin-coated film (0.09) shown in Figure S5, indicating that the CsPbBr<sub>3</sub> NF prepared by the monolayer PS sphere confined growth method can effectively suppress the growth of the (100) orientation and promote the growth along (110) orientation. For the preferred orientation of the CsPbBr<sub>3</sub> NFs as a function of the size of PS spheres, we think it is related to the longitudinal plane of the nanonet. With the increase of the diameter of the balls, more CsPbBr<sub>3</sub> precursor solution will be limited to the space

among the PS spheres and a bigger longitudinal plane is formed, resulting in a stronger (110) orientation.

In addition to improve the film morphology and crystallinity, the ordered nanonet-array structure also help boost the optical absorption. Figure 3b shows the absorbance spectra of the CsPbBr<sub>3</sub> films, determined by the reflectance and transmittance spectra, as shown in Figure S6. It is clear that the nanonet-array structure has higher absorbance compared with the traditionally spin-coated CsPbBr<sub>3</sub> film at wavelengths below 525 nm. The higher light-harvesting performance (Figure 3c) for the nanonet film can be attributed to the lower reflection and the higher absorbance, enhanced by the nanonet structures.

Our (110) orientation preferred CsPbBr<sub>3</sub> NF encourages us to fabricate MSM structured PDs and investigate the relationship between the device performance and the perovskite crystal orientation. The current-voltage (I-V) curves of the PDs based on the CsPbBr<sub>3</sub> NFs prepared with various PS spheres are measured, and the detailed dark- and photo-current data is summarized in Figure 3d. All of the dark current values are almost the same with the nA level at 2V, and the photocurrent increases first and then decreases with increasing the PS sphere size. The best PDs were obtained by using the CsPbBr<sub>3</sub> NF prepared with 850-nm PS spheres, which shows the highest photocurrent and the on/off ratio, boosting the dynamic range of the PD.

Previous reports [21, 22] revealed that the activation energies of vacancies and halogen interstitial defects had been calculated by the theoretical simulation with the values of less than 1.00 eV. These defects could be driven with fairly low activation energies, mostly along their favorite migration paths in the diagonal of the (100), (010) and (001) planes, which coincide with the direction of the electric field applied to the device on the (110) surface. Therefore, the (110) surface is beneficial for the carrier transport. Besides, lower Br<sup>-</sup> vacancy density was existed in the (110) lattice plane, which benefits for the charge carrier transport due to less recombination centers, less carrier traps, and less scattering while the carriers are drifting to the electrodes [24]. Finally, non-radiative recombination process is suppressed greatly by the applied

electric field [25], resulting in the larger photocurrent. Therefore, the stronger the (110) lattice plane, more favorable the carrier transport. Our results show that enhancing the intensity of the (110) lattice plane leads to increasing photocurrents in the PDs. When the diameter of the PS spheres is larger than 850 nm, although the peak ratio of  $I_{(110)}/I_{(100)}$  increases, especially for the 1150-nm PS spheres, the actual intensity of the (110) peak does not show a significant increase (Figure S3), which indicates that enhancing the intensity of the (110) orientation plays a more important role than suppressing the (100) intensity. Besides, for the CsPbBr<sub>3</sub> NFs prepared by using the PS spheres with the diameter larger than 850 nm, their optical absorption (Figure S7) is reduced because of the enlarged nanoholes. The increased pore-size results in less photoactive volume for the perovskite films, resulting in lower photocurrent and lower device performance. Therefore, the best CsPbBr<sub>3</sub> NF device is obtained by using the 850-nm PS spheres.

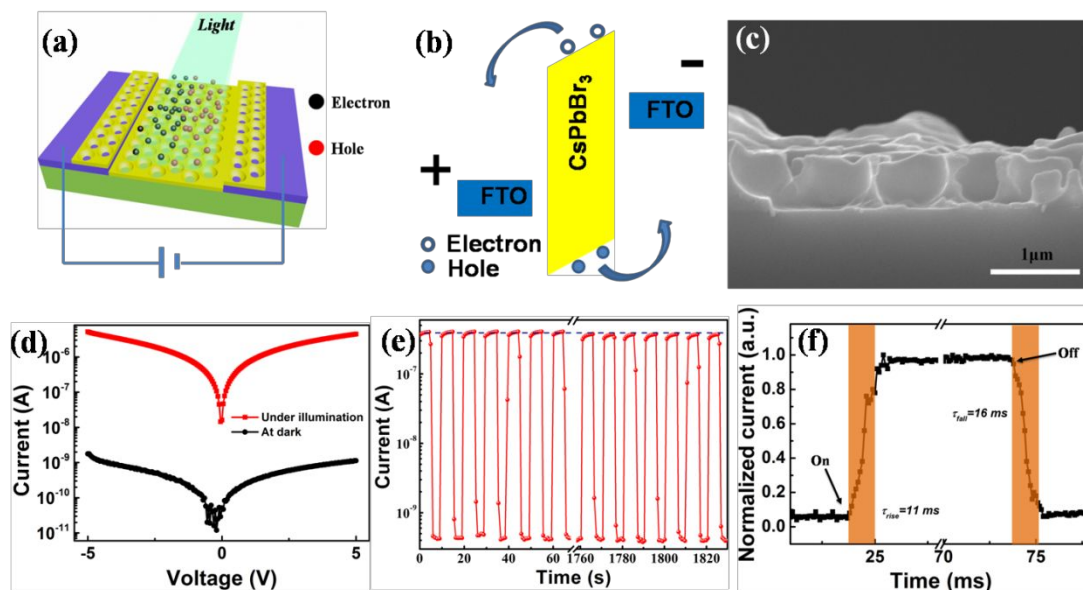


Figure 4 Schematic illustration (a) The perovskite NF PD (b) and energy band diagram of the perovskite NF PD. (c) Cross-sectional SEM image of the CsPbBr<sub>3</sub> NF prepared by using 850 nm PS spheres. (d) I-V curves of the PD. The optical power of a 473 nm laser is 145.8 mW cm<sup>-2</sup>. (e) current-time (I-t) curve of the PD without encapsulation in air for 30 min. The optical power of a 473 nm laser is 1.4 mW cm<sup>-2</sup>.

(f) Time response of the PD.

We further investigated the optimized CsPbBr<sub>3</sub> NF PDs in detailed performance analysis. Figure 4a and 4b show the schematic illustration and energy band diagram of the perovskite NF PD, respectively. Under the illumination of a 473 nm laser, the electron-hole pairs are generated in the CsPbBr<sub>3</sub> perovskite and the photogenerated carriers will be separated under an external bias voltage. The electrons reach the positive electrode and holes go to negative electrode, forming the photocurrent. Figure 4c shows the distinct section of the CsPbBr<sub>3</sub> NF with a thickness of about 570 nm and many nanoholes can be seen clearly. The I-V curves are shown in Figure 4d and the photocurrent increases significantly when the PD is illuminated under a 473 nm laser (145.8 mW cm<sup>-2</sup>), from which the on/off ratio can be calculated to be  $3.9 \times 10^3$  at 5 V, which is much larger than that of the device using the traditionally spin-coated film (~740), as shown in Figure S8. Furthermore, decent stability and superior repeatability have been seen from current-time measurements in air, as shown in Figure 4e. No obvious degradation was observed after 30 min measurements in air. In addition, the performance of the device after storage for 20 days in air is shown in Figure S9, which shows that the device has less than 1% degradation after 20 days in air. The above results demonstrate our devices have a decent stability. The normalized current versus time curve of the CsPbBr<sub>3</sub> NF PD is shown in Figure 4f, from which the response time can be calculated with the rise and fall times of 11 and 16 ms, respectively.

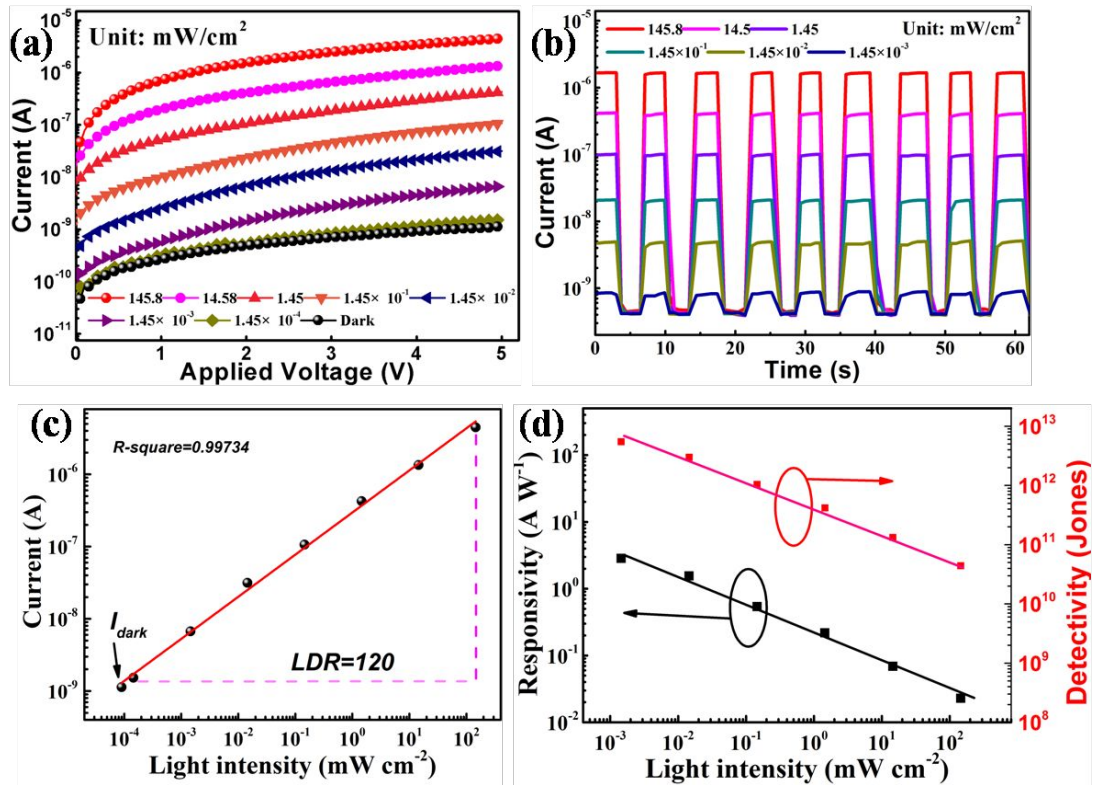


Figure 5 Device performance of the CsPbBr<sub>3</sub> NF PDs prepared by using 850 nm PS spheres. (a) I-V curves of the PD with various light intensities. (b) I-t curves of the PD with various light intensities. (c) Current versus light intensity curve. The LDR of the PD is 120 dB at 5 V bias. (d) Responsivity and detectivity of the PD.

Moreover, the I-V and I-t curves of a CsPbBr<sub>3</sub> NF PD prepared by using 850 nm PS spheres under illumination at various light intensities are shown in Figure 5a and 5b, respectively, which display obviously distinguishable characteristics. It can be seen clearly that with increasing the optical power from  $1.45 \times 10^{-4}$  to  $145.8 \text{ mW cm}^{-2}$ , the photocurrent increases distinguishably, which is very valuable for the PD to work under different lighting conditions.

As a figure-of-merit of the PD, the LDR is an important parameter for characterizing the light intensity range, which is always expressed as [26]

$$LDR = 20 \log \frac{P_{sat}}{P_{low}} \quad (1)$$

where  $P_{sat}$  ( $P_{low}$ ) is the optical power when the incident light intensity stronger (weaker) than which the photocurrent begins to deviate from linearity. The LDR of

the CsPbBr<sub>3</sub> NF PD prepared by using 850 nm PS spheres is measured by recording the photocurrent of the devices under the 473 nm laser with various light intensities modulated by neutral density optical filters, which is shown in Figure 5c. By linearly fitting the data, the *R*-squared (coefficient of determination) of the linear fitting for the CsPbBr<sub>3</sub> NF PD is 0.99734, which is slightly larger than that (0.97844) of the traditionally spin-coated CsPbBr<sub>3</sub> film device shown in Figure S11a, indicating the more perfect linearity of the data in the CsPbBr<sub>3</sub> NF PD. In addition, it can be seen that the current of the CsPbBr<sub>3</sub> NF PD has a linear response from  $1.45 \times 10^{-4}$  to 145.8 mW cm<sup>-2</sup>, corresponding to a LDR of 120 dB, which is larger than that (100 dB) of the traditionally spin-coated CsPbBr<sub>3</sub> film device and comparable with other perovskite-based PDs (Table S1).

Figure 5d shows the responsivity and detectivity of the PD prepared by using 850 nm PS spheres. From the figure, when the light intensity increases from  $10^{-3}$  to  $10^2$  mW cm<sup>-2</sup>, the responsivity and detectivity show a linear decrease trend. Under illumination with the light intensity of  $1.45 \times 10^{-3}$  mW cm<sup>-2</sup>, our device shows biggest responsivity and detectivity with the value of 2.84 A W<sup>-1</sup> and  $5.47 \times 10^{12}$  Jones (1 Jones = 1 cm Hz<sup>1/2</sup> W<sup>-1</sup>), respectively, all of which are larger than those of the traditionally spin-coated CsPbBr<sub>3</sub> film device, as shown in Figure S11b (0.027 A W<sup>-1</sup> and  $8.06 \times 10^{10}$  Jones).

In summary, the monolayer nano-PS sphere confined growth method was used to obtain CsPbBr<sub>3</sub> films with the preferred (110) orientation. The PDs based on (110)-orientation-preferred CsPbBr<sub>3</sub> NF prepared by using 850 nm PS spheres showed the best performance. The best-performing PD displayed the biggest LDR of up to 120 dB. Besides, the responsivity and detectivity of 2.84 A W<sup>-1</sup> and  $5.47 \times 10^{12}$  Jones were also achieved. Furthermore, our (110)-orientation-preferred CsPbBr<sub>3</sub> NF based PDs showed the better performance in all in all figures of merit than the device based on traditionally spin-coated CsPbBr<sub>3</sub> film device.

## Experimental Sections

### *Preparation of PS spheres*

2.4 g polyvinylpyrrolidone (PVP), 0.06 g 2,2'-Azobisisobutyronitrile (AIBN) and 3.25 g Styrene were put into a four-necked flask with 40 g Ethanol and were stirred at 300 rpm with nitrogen for 2 h. Then the flask was heated up to 70 °C while stirring at 100 rpm for 24 h. After that the white product was obtained and centrifuged, washed several times with ethanol. Finally, the product was dispersed in ethanol for use. To obtain the PS spheres with smaller diameter, the amount of PVP in the solution will be increased, or increasing the ratio of AIBN or styrene will increase the diameter of the PS spheres.

#### *Monolayer PS sphere preparation*

In a 25-cm depth circular glass tank with the deionized water filled to 10 cm, 200  $\mu$ L PS ethanol solution was dropped in the center of the water surface by using a plastic pipette. Until the PS solution spread uniformly on the water surface, 1 mL SDS solution (10 WT%) was dropped along the edge of the glass tank. Then, an ultraviolet ozone treated FTO substrate with a channel of 3.5 $\times$ 0.08 mm<sup>2</sup> was inserted into the water under the PS layer from the edge of the PS layer, and slowly picked up vertically. After that, the FTO coated by the monolayer PS spheres was placed on a hot plate to heat up to 50 °C and keep for 1 h.

#### *Preparation of the CsPbBr<sub>3</sub> nanonet Film PDs*

0.1064 g cesium bromide (99.999%) and 0.263 g lead bromide (99.99%) were dissolved in 1 mL DMSO (99.9%) and allowed to stand for 24 h. The 70  $\mu$ L filtered CsPbBr<sub>3</sub> precursor solution (0.5 mol/L) was added drop by drop on the PS coated FTO substrate, and spin-coated at 1500 rpm for 40 s, and then baked on a hot plate at 100 °C for 30 min. After it was cooled down, it was immersed in a bottle filled with chlorobenzene for 1 minute to remove the PS spheres. After taking out, it was baked at 100°C for 30 min to remove chlorobenzene. Finally, the CsPbBr<sub>3</sub> nanonet film PDs with an active area of 3.5 $\times$ 0.08 mm<sup>2</sup> were prepared.

#### *Preparation of the traditionally spin-coated CsPbBr<sub>3</sub> film PDs*

0.1064 g cesium bromide (99.999%) and 0.263 g lead bromide (99.99%) were dissolved in 1 mL DMSO (99.9%) to form 0.5 mol/L perovskite precursor solution and stood for 24 h. Then, 70  $\mu$ L filtered CsPbBr<sub>3</sub> precursor solution was added drop by drop on the FTO substrate, and spin-coated at 1500 rpm for 40 s. The resulting film was then annealed at 100 °C for 30 min. Finally, the CsPbBr<sub>3</sub> film PDs with an active area of 3.5×0.08 mm<sup>2</sup> were prepared.

### *Characterization*

High-resolution SEM images were measure by field emission scanning electron microscopy (FESEM,JEOL, JSM-6700F), XRD patterns were performed by using D8 FOCUS X-ray diffraction and absorption spectra were taken by UV-Vis spectrophotometer. The I-V and I-t curves were measured by an AgilentB1500 electrometer. An oscilloscope was used to characterize the fast response time of our devices. A 473 nm laser (50 mW) was used as the light source and its optical power was calibrated by a standard Si diode.

## ACKNOWLEDGEMENTS

This work at Hubei University is supported by the National Natural Science Foundation of China (No. 11874143), and the work is also financially supported by the Office of Naval Research under Contract no. N00014-17-1-2223, Air Force Research Laboratory under Space Vehicles Directorate (FA9453-11-C-0253), and the Ohio Research Scholar Program.

## ASSOCIATED CONTENT

The Supporting Information is available on the website including experimental figures and table.

## REFERENCES

- (1) Green, M. A.; Hishikawa, Y.; Dunlop, E. D.; Levi, D. H.; Hohl-Ebinger, J.; Ho-Baillie. Solar Cell Efficiency Table (Version 51), *Prog. Photovol.* **2018**, *26*, 3-12.
- (2) Lin, K.; Xing, J.; Quan, L. N.; de Arquer, F. P. G.; Gong, X.; Lu, J.; Xie, L.; Zhao, W.; Zhang, D.; Yan, C.; Li, W.; Liu, X.; Lu, Y.; Kirman, J.; Sargent, E. H.; Xiong, Q.; Wei, Z. Perovskite Light-Emitting Diodes with External Quantum Efficiency Exceeding 20 Per Cent. *Nature.* **2018**, *562*(7726), 245.
- (3) Cao, Y.; Wang, N.; Tian, H.; Guo, J.; Wei, Y.; Chen, H.; Miao, Y.; Zou, W.; Pan, K.; He, Y.; Cao, H.; Ke, Y.; Xu, M.; Wang, Y.; Yang, M.; Du, K.; Fu, Z.; Kong, D.; Dai, D.; Jin, Y.; Li, G.; LI, H.; Peng, Q.; Wang, J.; Huang, W. Perovskite Light-Emitting Diodes Based on Spontaneously Formed Submicrometre-Scale Structures. *Nature.* **2018**, *562*, 249-253.
- (4) Feng, J.; Gong, C.; Gao, H.; Wen, W.; Gong, Y.; Jiang, X.; Zhang, B.; Wu, Y.; Wu, Y.; Fu, H.; Jiang, L.; Zhang, X. Single-Crystalline Layered Metal-Halide Perovskite Nanowires for Ultrasensitive Photodetectors, *Nature Electronics.* **2018**, *1*, 404-410.
- (5) Xue, J.; Zhu, Z.; Xu, X.; Gu, Y.; Wang, S.; Xu, L.; Zou, Y.; Song, J.; Zeng, H.; Chen, Q. Narrowband Perovskite Photodetector-Based Image Array for Potential Application in Artificial Vision, *Nano Lett.* **2018**, *18* (12), 7628–7634.
- (6) Song, J.; Cui, Q.; Li, J.; Xu, J.; Wang, Y.; Xu, L.; Xue, J.; Dong, Y.; Tian, T.; Sun, H.; Zeng, H. Ultralarge All-Inorganic Perovskite Bulk Single Crystal for High-Performance Visible–Infrared Dual-Modal Photodetectors. *Adv. Opt. Mater.* **2017**, *5*, 1700157.
- (7) Zhang, X.; Yang, S.; Zhou, H.; Liang, J.; Liu, H.; Xia, H.; Zhu, X.; Jiang, Y.; Zhang, Q.; Hu, W.; Zhuang, X.; Liu, H.; Hu, W.; Wang, X.; Pan, A. Perovskite–Erbium Silicate Nanosheet Hybrid Waveguide Photodetectors at the Near - Infrared Telecommunication Band. *Adv. Mater.* **2017**, *29*, 1604431.
- (8) Hu, X.; Zhou, H.; Jiang, Z.; Wang, X.; Yuan, S.; Lan, J.; Fu, Y.; Zhang, X.; Zheng, W.; Wang, X.; Zhu, X.; Liao, L.; Xu, G.; Jin, S.; Pan, A. Direct Vapor

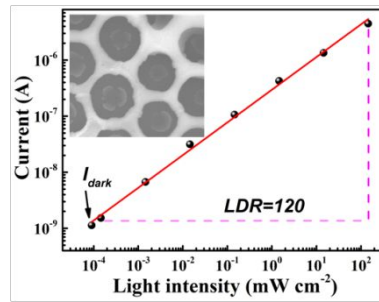
- Growth of Perovskite CsPbBr<sub>3</sub> Nanoplate Electroluminescence Devices. *ACS Nano*. **2017**, *11*, 9869-9876.
- (9) Li, Y.; Shi, Z. F.; Li, S.; Lei, L. Z.; Ji, H. F.; Wu, D.; Xu, T.; Tian, Y.; Li, X. J. High-performance perovskite photodetectors based on solution-processed all-inorganic CsPbBr<sub>3</sub> thin films. *J. Mater. Chem. C*. **2017**, *5*(33), 8355-8360.
- (10) Li, Y.; Shi, Z.; Lei, L.; Ma, Z.; Zhang, F.; Li, S.; Xu, T.; Li, X.; Shan, C.; Du, G. Controllable Vapor-Phase Growth of Inorganic Perovskite Microwire Networks for High-Efficiency and Temperature-Stable Photodetectors. *ACS Photonics*. **2018**, *5*(6), 2524-2532.
- (11) Yang, Z.; Xu, Q.; Wang, X.; Lu, J.; Wang, H.; Li, F.; Zhang, L.; Hu, G.; Pan, C. Large and Ultrastable All - Inorganic CsPbBr<sub>3</sub> Monocrystalline Films: Low - Temperature Growth and Application for High-Performance Photodetectors. *Adv. Mater.* **2018**, *30*(44), 1802110.
- (12) Ding, J.; Du, S.; Zuo, Z.; Zhao, Y.; Cui, H.; Zhan, X. High Detectivity and Rapid Response in Perovskite CsPbBr<sub>3</sub> Single-Crystal Photodetector. *J. Phys. Chem. C*. **2017**, *121*(9), 4917-4923.
- (13) Saidaminov, M. I.; Haque, M. A.; Almutlaq, J.; Sarmah, S.; Miao, X.H.; Begum, R.; Zhumekenov, A.A.; Dursun, I.; Cho, N.; Murali, B.; Mohammed, O.F.; Wu, T.; Bakr, O.M. Inorganic Lead Halide Perovskite Single Crystals: Phase-Selective Low - Temperature Growth, Carrier Transport Properties, and Self - Powered Photodetection. *Adv. Opt. Mater.* **2017**, *5*, 1600704.
- (14) Rao, H.; Li, W.; Chen, B.; Kuang, D.; Su, C. In Situ Growth of 120 cm<sup>2</sup> CH<sub>3</sub>NH<sub>3</sub>PbBr<sub>3</sub> Perovskite Crystal Film on FTO Glass for Narrowband-Photodetectors. *Adv. Mater.* **2017**, *29*, 1602639.
- (15) Rao, H.; Chen, B.; Wang, X.; Kuang, D.; Su, C. A Micron-Scale Lamellar MAPbBr<sub>3</sub> Single Crystal for An Efficient and Stable Perovskite Solar Cell. *Chem. Comm.* **2017**, *53*, 5163.
- (16) Cho, H.; Wolf, C.; Kin, J.S.; Yun, H.J.; Bae, J.S.; Kim, H.; Heo, J-M.; Ahn, S.; Lee, T-W. High-Efficiency Solution-Processed Inorganic Metal Halide

- Perovskite Light-Emitting Diodes. *Adv. Mater.* **2017**, *29*, (31).
- (17) Wolf, C.; Lee, T-W. Exciton and Lattice Dynamics In Low-Temperature Processable CsPbBr<sub>3</sub> Thin-Films. *Mater. Today Energ.* **2018**, *7*, 199-207.
- (18) Zeng, J.; Li, X.; Wu, Y.; Yang, D.; Sun, Z.; Song, Z.; Wang, H.; Zeng, H. Space-Confined Growth of CsPbBr<sub>3</sub> Film Achieving Photodetectors with High Performance in All Figures of Merit. *Adv. Funct. Mater.* **2018**, *28*(43), 1804394.
- (19) Yantara, N.; Bhaumik, S.; Yan, F.; Sabba, D.; Dewi, H.A.; Mathews, N.; Boix, P.P.; Demir, H.V.; Mhaisalkar, S. Inorganic halide perovskites for efficient light-emitting diodes. *J. Phys. Chem. Lett.* **2015**, *6*(21), 4360-4364.
- (20) Sutton, R.J.; Eperon, G.E.; Miranda, L.; Parrott, E.S.; Kamino, B.A.; Patel, J.B.; Hörantner, M.T.; Johnston, M.B.; Haghighirad, A.A.; Moore, D.T.; Snaith, H.J. Bandgap - tunable cesium lead halide perovskites with high thermal stability for efficient solar cells. *Adv. Energ. Mater.* **2016**, *6*(8), p.1502458.
- (21) Chang, X.; Li, W.; Zhu, L.; Liu, H.; Geng, H.; Xiang, S.; Liu, J.; Chen, H. Carbon-Based CsPbBr<sub>3</sub> Perovskite Solar Cells: All-Ambient Processes and High Thermal Stability. *ACS Appl. Mater. Inter.* **2016**, *8*(49), 33649-33655.
- (22) Azpiroz, J. M.; Mosconi, E.; Bisquert, J.; De Angelis, F. Defects Migration in MethylAmmonium Lead Iodide and their Role in Perovskite Solar Cells Operation. *Energ. Environ. Sci.* **2015**, *8*, 2118-2127.
- (23) Zuo, Z.; Ding, J.; Zhao, Y.; Du, S.; Li, Y.; Zhan, X.; Cui, H. Enhanced Optoelectronic Performance on The (110) Lattice Plane of An MAPbBr<sub>3</sub> Single Crystal. *J. Phys. Chem. Lett.* **2017**, *8*(3), 684-689.
- (24) Wang, W.; Ma, Y.; Qi, L. High - Performance Photodetectors Based on Organometal Halide Perovskite Nanonets. *Adv. Func. Mater.* **2017**, *27*(12), 1603653.
- (25) Du, M.H. Efficient Carrier Transport in Halide Perovskites: Theoretical Perspectives. *J. Mater. Chem. A.* **2014**, *2*, 9091-9098.
- (26) Tress, W.; Marinove, N.; Inganas, O.; Nazeeruddin, M. K.; Zakeeruddin, S. M.; Graetzel, M. Predicting the Open-Circuit Voltage of CH<sub>3</sub>NH<sub>3</sub>PbI<sub>3</sub> Perovskite Solar Cells Using Electroluminescence and Photovoltaic Quantum Efficiency

Spectra: the Role of Radiative and Non-Radiative Recombination. *Adv. Energ. Mater.* **2014**, *5*, 1400812.

- (27) Bao, C.; Chen, Z.; Fang, Y.; Wei, H.; Deng, Y.; Xiao, X.; Li, L.; Huang, J. Low - Noise and Large - Linear - Dynamic - Range Photodetectors Based on Hybrid - Perovskite Thin - Single - Crystals. *Adv. Mater.* **2017**, *29*(39), 1703209.

### A table of contents entry



A photodetector based on (110)-orientation-preferred CsPbBr<sub>3</sub> nanonet films with ordered nanostructures displayed the high device performance.